Journal of Solid State Chemistry 184 (2011) 2525–2532

Contents lists available at ScienceDirect

Journal of Solid State Chemistry

journal homepage: www.elsevier.com/locate/jssc

Phase composition and magnetic properties of niobium–iron codoped TiO_2 nanoparticles synthesized in Ar/O_2 radio-frequency thermal plasma

Chenning Zhang [a,b], Masashi Ikeda [a,c], Masaaki Isobe [d], Tetsuo Uchikoshi [a], Ji-Guang Li [a], Takayuki Watanabe [b], Takamasa Ishigaki [e,a,*]

[a] Materials Processing Unit, National Institute for Materials Science, Tsukuba, Ibaraki 305-0047, Japan
[b] Department of Environmental Chemistry and Engineering, Tokyo Institute of Technology, Yokohama, Kanagawa, 226-8502, Japan
[c] Department of Materials Chemistry, Hosei University, Koganei, Tokyo 184-8584, Japan
[d] Superconducting Properties Unit, National Institute for Materials Science, Tsukuba, Ibaraki 305-0044, Japan
[e] Department of Chemical Science and Technology, Hosei University, Koganei, Tokyo 184-8584, Japan

ARTICLE INFO

Article history:
Received 11 March 2011
Received in revised form
12 July 2011
Accepted 14 July 2011
Available online 22 July 2011

Keywords:
Anatase
Rutile
Ferromagnetic
Paramagnetic
Carrier-mediated exchange

ABSTRACT

Nanoparticles of Nb^{5+}–Fe^{3+} codoped TiO_2 with various Nb^{5+} concentrations (Nb/(Ti+Fe+Nb)=0–10.0 at%) and Fe^{3+} (Fe/(Ti+Fe+Nb)=0–2.0 at%) were synthesized using Ar/O_2 thermal plasma. Dopant content, chemical valence, phase identification, morphology and magnetic properties were determined using several characterization techniques, including inductively coupled plasma-optical emission spectrometer, X-ray photoelectron spectroscopy, X-ray diffraction, UV–vis diffuse reflectance spectrometer, field-emission scanning electron microscopy, transmission electron microscopy and SQUID commercial instrument. The XRD revealed that all the plasma-synthesized powders were exclusively composed of anatase as major phase and rutile. The rutile weight fraction was increased by the substitution of Fe^{3+} for Ti^{4+} whereas it was reduced by the Nb^{5+} doping. The plasma-synthesized Nb^{5+}–Fe^{3+} codoped TiO_2 powders had intrinsic magnetic properties of strongly paramagnetic and feebly ferromagnetic at room temperature. The ferromagnetic properties gradually deteriorated as the Fe^{3+} concentration was decreased, suggesting that the ferromagnetism was predominated by the phase composition as a carrier-mediated exchange.

1. Introduction

Recently, the emergence of spintronic devices has enabled faster processing and larger storage capacity to meet the increasing demand for information technology [1–5]. For the use as spintronic materials, dilute magnetic semiconductors (DMS) have gained considerable attention as the spin injectors for spintronic devices [5–10]. A DMS is typically a nonmagnetic semiconductor doped with a few to several atomic percent of an open-shell transition metal [11]. The transition metal atoms are introduced into the semiconductor host lattice, thus enabling local magnetic moments to be inserted into the lattice.

Doping transition metal ions into semiconductor oxides to induce the room-temperature ferromagnetism (RTF) performance in the DMS materials has been used in potential application to spintronic devices, since RTF in codoped TiO_2 was found by Matsumoto et al. [12–14]. TiO_2 as one of the promising hosts for the DMS materials have exhibited many technologically attractive physical and chemical properties, such as high refractive index, excellent optical transmittance in the visible wavelength region, high dielectric constant and remarkable photocatalysis [15]. Anatase (tetragonal, space group D_{4h}^{19}) and rutile (tetragonal, space group D_{4h}^{14}), two common modifications of TiO_2, have quite different arrangements of their structural building blocks (Ti–O octahedrons) [16]. Owing to their different featured structure, their some properties demonstrate big divergence in terms of theoretical density, refractive index, band gap and, particularly, carrier mobility [17]. Hitosugi et al. [18] pronounced that the charge carriers in Nb-doped Co–TiO_2 and Fe–TiO_2 epitaxial thin films fabricated using pulsed laser deposition technique are spin polarized and that they could be used to mediate the ferromagnetic interaction between the local spins on the transition metal ions by adjusting the Nb^{5+} doping. In other words, the ferromagnetism is sensitive to the carrier concentration, which depends on the Nb^{5+} concentration. Up to date, the origin of RTF as one issue has remained under debate. A number of reports pronounced that the RTF has intrinsic nature [19–22], whereas other claimed that it is extrinsic due to the existence of the isolated metallic clusters of doping elements as a result of

* Corresponding author at: Department of Chemical Science and Technology, Hosei University, Koganei, Tokyo 184-8584, Japan. Fax: +81 42 387 6134.
E-mail address: ishigaki@hosei.ac.jp (T. Ishigaki).

0022-4596/$ - see front matter © 2011 Elsevier Inc. All rights reserved.
doi:10.1016/j.jssc.2011.07.025

synthesis under high vacuum or in reducing atmosphere [23–27]. Therefore, the understanding for the RTF origin should heavily depend upon the methods and the conditions of sample preparation.

In contrast to conventional synthetic routs, radio-frequency (RF) thermal plasma synthesis is characterized by extremely high temperature (up to ~15,000 K), enhanced reactivity due to the high concentrations of chemically reactive radicals, and superfast quenching rate (~10^5–10^6 K/s) in the plasma tail flame region [28]. These salient characteristics make it better suited than conventional wet-chemical methods for synthesizing nanoparticles with good crystallinity and a homogeneous dopant distribution within short time. Wang et al. [29] synthesized Fe^{3+}-doped TiO_2 nanoparticles with controlled $R_{Fe/Ti}$ ranging from nominally zero to 20% using oxidative pyrolysis of liquid precursors via Ar/O_2 RF thermal plasma synthesis. All the as-prepared Fe^{3+}-doped TiO_2 nanoparticles were strongly paramagnetic in nature at room temperature. Li et al.[30] clarified the origin of RTF using the Ar/O_2 RF thermal plasma to synthesize Co^{2+}-doped TiO_2 nanoparticles. The resultant powder did not contain any metallic Co or other ferromagnetic impurities because of the oxidative atmosphere in the synthesis process, meaning that the RTF properties of the plasma-synthesized powders had an intrinsic nature.

In the work reported here, we synthesized Nb^{5+}–Fe^{3+} codoped TiO_2 nanoparticles using Ar/O_2 RF thermal plasma oxidizing liquid precursor mist. We found that the magnetic properties of strong paramagnetic and weak ferromagnetic in the plasma-synthesized powders as intrinsic nature, the rutile weight fraction in the plasma-generated powders was promoted by the substitution of Fe^{3+} for Ti^{4+} whereas it was inhibited by the Nb^{5+} doping, and ferromagnetism was affected by the amount of rutile in the phase composition as a carrier-mediated exchange. In the following sections, we describe the synthesis process and characterization techniques, examine the chemical analysis and valence determination, and discuss the phase composition and magnetic properties of the plasma-synthesized Nb^{5+}–Fe^{3+} codoped TiO_2 powders.

2. Experimental details

All the chemicals used in this work were reagent grade supplied by Wako Pure Chemical Industry Ltd., Tokyo, Japan, and were used as received. Liquid precursor was prepared by adding, under continuous magnetic stirring, 0.1 mol of titanium (IV) tetrabutylate ($Ti(OBu)_4$) to 0.4 mol of diethanolamine ($HN(OC_2H_5)_2$), a chelate for Ti^{4+} that prevents hydrolysis from occurring when water is intentionally added or when there is exposure to moisture (solution I). Separately, niobium (V) pentapropylate ($Nb(OPr)_5$) was injected into the ($HN(OC_2H_5)_2$ chelate against the hydrolysis at a molar ratio of 1:5, with a target Nb^{5+} content of Nb/(Ti+Fe+Nb)=0–10.0 at% (solution II). Preweighed ferrocene (II) ($Fe(C_5H_5)_2$) was dissolved, under continuous magnetic stirring, in ethanol (C_2H_5OH) at a nominal concentration of Fe/(Ti+Fe+Nb)=0–2.0 at% (solution III). Mixing solutions I, II and III produced a stable clear liquid precursor solution.

The experimental apparatus used to synthesize powder are primarily composed of a water-cooled induction plasma torch (model PL-50, TEKNA Plasma System Inc., Sherbrooke, QC, Canada), a water-cooled atomizer probe (model SA792-260-100, TEKNA Plasma System Inc., Sherbrooke, QC, Canada), 2 MHz, 40 kW RF power supply system (Nihon Koshuha Co. Ltd., Yokohama, Japan), a water-cooled stainless steel reactor, a stainless steel filter connecting the reactor and a vacuum pump for maintaining reactor pressure. The liquid precursor was delivered by a peristaltic pump into the center of the plasma plume through an atomization probe at the top of the plasma reactor in a mist state. The instantaneous oxidation of the liquid precursor mist by the O_2 in the plasma sheath formed nanoparticles. The details of the experimental setup is described elsewhere [31], and the conditions under which the thermal plasma was generated are summarized in Table 1.

Table 1
Experimental conditions for synthesizing the Nb^{5+}–Fe^{3+} codoped TiO_2 powders via Ar/O_2 thermal plasma.

Parameter	Value
Central gas, flow rate	Ar, 15 L/min
Sheath gas, flow rate	Ar, 60 L/min; O_2, 10 L/min
Atomization gas, flow rate	Ar, 5 L/min
Precursor feeding rate	3.0 mL/min
Induction power for plasma generation	~40 kW
Chamber pressure	~26.7 kPa

The Fe and Nb-codoped TiO_2 nanoparticles formed via instantaneous oxidation of the liquid precursor mists by the O_2 mixed in the sheath gas were collected from the inner wall of the reactor and the filter. The total collection yield was ~90% and the mass ratio of powder collected at the reactor inner wall to that collected on the filter was approximately 3:1. No significant difference was observed between the two kinds of nanoparticles, although much difference was reported in the thermal plasma spheroidization of micron-sized or tens-of-micron-sized particles, in which much smaller particle size was recognized in the particles collected on the filter than those collected at the reactor inner wall [32]. The characterization of main product of ~70% yield collected at the reactor inner wall is shown in this work.

2.1. Characterization techniques

The elemental concentrations of iron and niobium in the resultant powders were analyzed using a standard inductively coupled plasma-optical emission spectrometer (ICP-OES) (model SPS1700HVR, Seiko Instruments Inc., Chiba, Japan). The oxidation states of the titanium, niobium and iron in the plasma-generated powders were determined using a high-resolution X-ray photoelectron spectroscope (XPS) (model 5700, PHI, Chanhassen, MN, USA), with monochromatized Al$K\alpha$ irradiation (1486.6 eV) and an incident power of 200 W. The core-level binding-energy of Ti2$p_{3/2}$ (458.5 eV) was used as a reference to compensate for any electrostatic shifts resulting from sample charging during photoelectron measurement. The phase identification was performed using an X-ray diffractometer (XRD) (model RINT 2200, Rigaku, Tokyo, Japan), nickel-filtered Cu$K\alpha$ radiation at 40 kV/40 mA and a scanning speed of 0.5°/2θ per minute. The XRD patterns were obtained by baseline subtraction, Lorentz polarization correction and $K_{\alpha 2}$ stripping. The average crystallite sizes, D, of the rutile and anatase were estimated using the well-known Debye–Scherrer formula by analyzing broadened rutile (110) and anatase (101) diffraction peaks [33]:

$$D = \frac{K\lambda}{\beta \cos\theta} \quad (1)$$

where λ is the XRD wavelength (Cu$K\alpha$ λ=0.15405 nm), K is a shape factor taken as 0.89, β is the full-width at half maximum (FWHM) of the rutile (110) or anatase (101) diffraction peak and θ is the diffraction angle corresponding to the diffraction peak of the rutile (110) or anatase (101). The rutile weight fraction in the plasma-synthesized powders was estimated from the integrated intensities of the rutile (110) and anatase (101) diffraction peaks

in the XRD pattern, using the equation of Spurr and Myers [34]:

$$f_R = \frac{1}{(1+0.79(I_A/I_R))} \quad (2)$$

where f_R is the weight fraction of the rutile phase, and I_R and I_A are the integrated intensities of the rutile (110) and anatase (101) diffraction peaks, respectively. The absorption edge was determined by observing the ultraviolet-visible (UV–vis) absorption spectra on a spectrophotometer (model V-560, Jasco Co., Tokyo, Japan), using $BaSO_4$ for baseline calibration. The band gap energy (E_g) was calculated from the relationship between the absorption coefficient and the incident photon energy in the indirect semiconductor [31,35]:

$$\alpha = \frac{B_i(h\nu - E_g)^2}{h\nu} \quad (3)$$

$$A = \frac{\alpha}{B_i} \quad (4)$$

$$h\nu = \frac{1240}{\lambda} \quad (5)$$

where α is the absorption coefficient, $h\nu$ is the incident photon energy, B_i is the absorption constant for the indirect transitions and A is the absorption proportional to α. The band gap was obtained by extrapolating the linear parts of the curves in the plots of $(Ah\nu)^{1/2}$ versus $h\nu$. The particle morphology was observed using a field-emission scanning electron microscope (FE-SEM) (model S-5000, Hitachi, Tokyo, Japan) and a transmission electron microscope (TEM) (model JEM-2000 EX-II, acceleration voltage 200 kV, JEOL, Ltd., Tokyo, Japan). The lattice fringes of individual anatase and rutile were identified using a high-resolution transmission electron microscope (HRTEM) (model JEM-4000 EX acceleration voltage 400 kV, JEOL, Ltd., Tokyo, Japan). The magnetic properties were measured at room temperature using a SQUID commercial instrument (Model MPMS-XL, Quantum Design, San Diego, CA, USA).

3. Results and discussion

The results of ICP-OES (Table 2) show that the concentrations of iron and niobium in the synthesized powders were almost equivalent to the nominal concentrations in the precursor solutions, suggesting that the dopant contents were retained in the final products via the thermal plasma synthesis.

The high-resolution XPS spectra used for determining the oxidation states of (a) titanium, (b) niobium and (c) iron in the TiO_2–Fe^{3+} (2.0 at%)–Nb^{5+} (6.0 at%) sample as representative case are shown in Fig. 1. The Ti2p peaks (Fig. 1a) were characterized as Ti2$p_{3/2}$ (~457.9 eV) and Ti2$p_{1/2}$ (~463.8 eV) with a spin-orbital doublet splitting (Δ=Ti2$p_{1/2}$−Ti2$p_{3/2}$=~5.9 eV), suggesting an oxidation state of +4 for titanium [36,37]. The Nb3$d_{5/2}$ and Nb3$d_{3/2}$ ones (Fig. 1b) locating at ~207.8 and ~210.8 eV, respectively, correspond to the reported values for Nb^{5+} in Nb_2O_5 [38–40]. These results mean that the +4 oxidation state for Ti and the +5 one for Nb in the precursor solution were maintained in the plasma-synthesized powders, which we attribute to the uses of an oxygen atmosphere in the synthesis process. In contrast, characteristic Fe2p peaks (Fig. 1c) appear in several shake-up satellite peaks, probably due to the low doping concentration. It is thus very difficult to reliably identify the chemical valence of iron in the resultant powder by referring the 722.8 eV of Fe2$p_{1/2}$ and 709.8 eV of Fe2$p_{3/2}$ for Fe^{2+} and the 724.3 eV of Fe2$p_{1/2}$ and 711.2 eV of Fe2$p_{3/2}$ for Fe^{3+} in the Fe2p spectra obtained from the reference FeO and Fe_2O_3 samples [41]. However, it can find an indication from previous work [29] that the iron doped in TiO_2 via the Ar/O_2 thermal plasma synthesis was determined to have an oxidation state of +3 on the basis of the isomer shift and the quadrupole splitting from Mössbauer spectra. This was ascribed to the oxidative effect of the thermal plasma synthesis. Thus, in this work, the oxidative atmosphere created by injecting O_2 into the plasma reactor during the synthesis process should have given the Fe atoms in the TiO_2 an oxidation state of +3. Moreover, the finding that the metallic Fe2p peaks, reported values of 719.8 eV of Fe2$p_{1/2}$ and 706.8 eV of Fe2$p_{3/2}$ for Fe^0 in pure iron [41], in the XPS spectra (Fig. 1c) were almost imperceptible, indicating the absence of Fe metal phase in the plasma-synthesized powder.

The XRD patterns of the plasma-generated powders are exhibited in Fig. 2: (a) TiO_2–Fe^{3+} (0–2.0 at%), (b) TiO_2–Fe^{3+} (0.1–2.0 at%)–Nb^{5+} (2.0 at%) and (c) TiO_2–Fe^{3+} (0.1–2.0 at%)–Nb^{5+} (6.0 at%). The unambiguous diffraction peaks indicate that the resultant powders had high crystallinity, owing to the extremely high synthesis temperature (up to ~15,000 K) during the thermal plasma processing. In such case, it saved the postannealing step frequently required to obtain good crystalline quality in many wet-chemical techniques. In Fig. 2(d), an enlarged XRD pattern (with the ten-times more enlarged Y-axis scale than those in Fig. 2(a)–(c)) is shown to confirm the formation of no other phase than rutile and anatase. Through phase identification, mixed polymorphs of anatase (JCPDS: No. 84-1286) as a major phase and rutile (JCPDS: No. 78-2485) were exclusively observed in all the plasma-synthesized samples, without any metal or magnetic impurity phases, which is in agreement with the determination made using the XPS spectra (Fig. 1). This mixed phase composition is understandable from the results of the thermodynamic calculation used to analyze the nucleation of the anatase and rutile from the TiO_2 melt using the estimated values of the interfacial energy between the condensed and liquid phases [42]. The calculations show that the metastable anatase was formed as main phase in a rapid cooling process, while the thermodynamically stable rutile was created in a less cooling condition. This difference is reasonable from a kinetic point of view based on classical homogeneous nucleation theory and also agrees with the experimental observation. This was due to the different temperature profiles in the thermal plasma and the complex trajectories of the precursor mists. Moreover, the different cooling process in the thermal plasma processing explains why the average crystallite size (30–40 nm) of the anatase was smaller than that (56–74 nm) of the rutile. The sizes were estimated using the nucleation aspect of these two phases and applying Eq. (1) to the plasma-synthesized powders including undoped TiO_2, TiO_2–Fe^{3+} (0.1–2.0 at%), TiO_2–Fe^{3+} (0.1–2.0 at%)–Nb^{5+} (2.0 at%) and TiO_2–Fe^{3+} (0.1–2.0 at%)–Nb^{5+} (6.0 at%). As mentioned earlier, the nucleation of the anatase from the deeply undercooled TiO_2 melts

Table 2
Elemental concentrations of iron and niobium in the precursor solutions and plasma-synthesized powders.

Nominal concentration in the precursor solutions		Measured concentration in the synthesized powders	
Fe (at%)	Nb (at%)	Fe (at%)	Nb (at%)
0.1	0.0	0.1	0.0
0.5	0.0	0.5	0.0
1.0	0.0	1.0	0.0
2.0	0.0	2.0	0.0
0.1	2.0	0.1	2.0
0.5	2.0	0.5	2.0
1.0	2.0	0.9	2.0
2.0	2.0	1.9	2.0
0.1	6.0	0.1	6.1
0.5	6.0	0.5	6.1
1.0	6.0	0.9	6.1
2.0	6.0	1.8	6.1

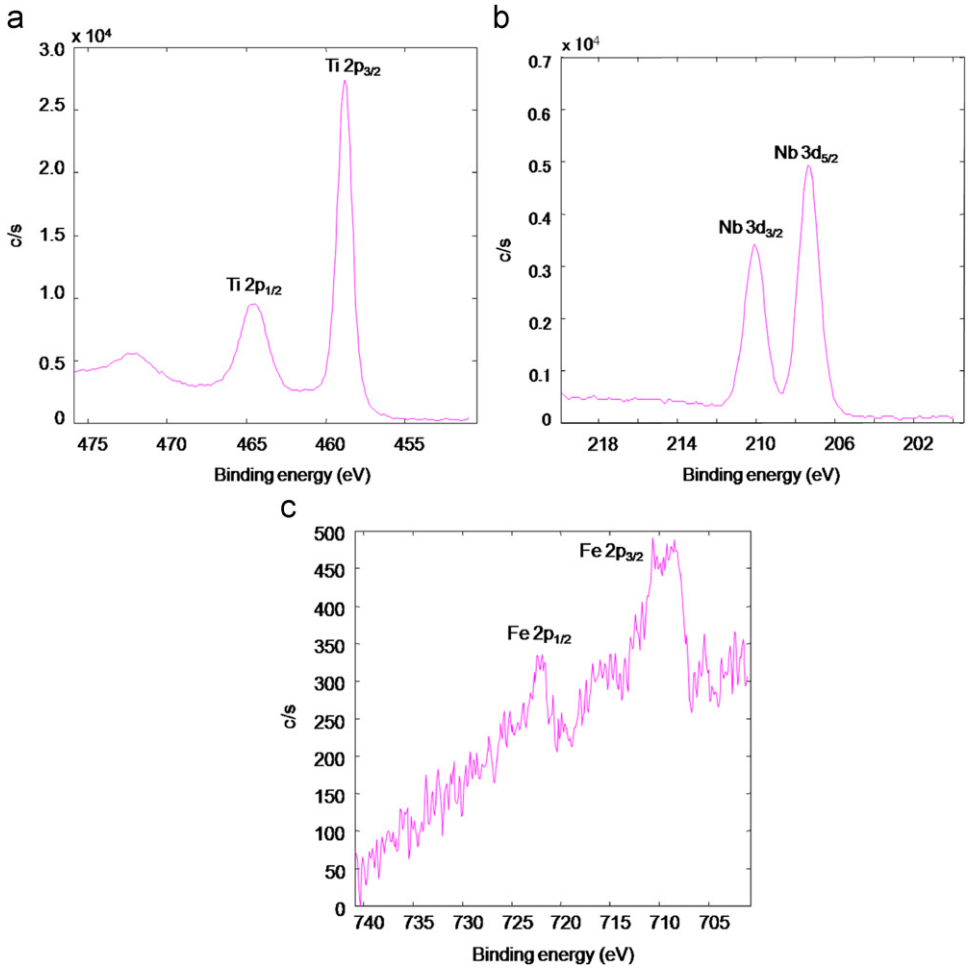

Fig. 1. High-resolution XPS spectra of the plasma-synthesized Nb^{5+}–Fe^{3+} codoped TiO_2 powders: (a) Ti2*p*, (b) Nb3*d* and (c) Fe2*p*.

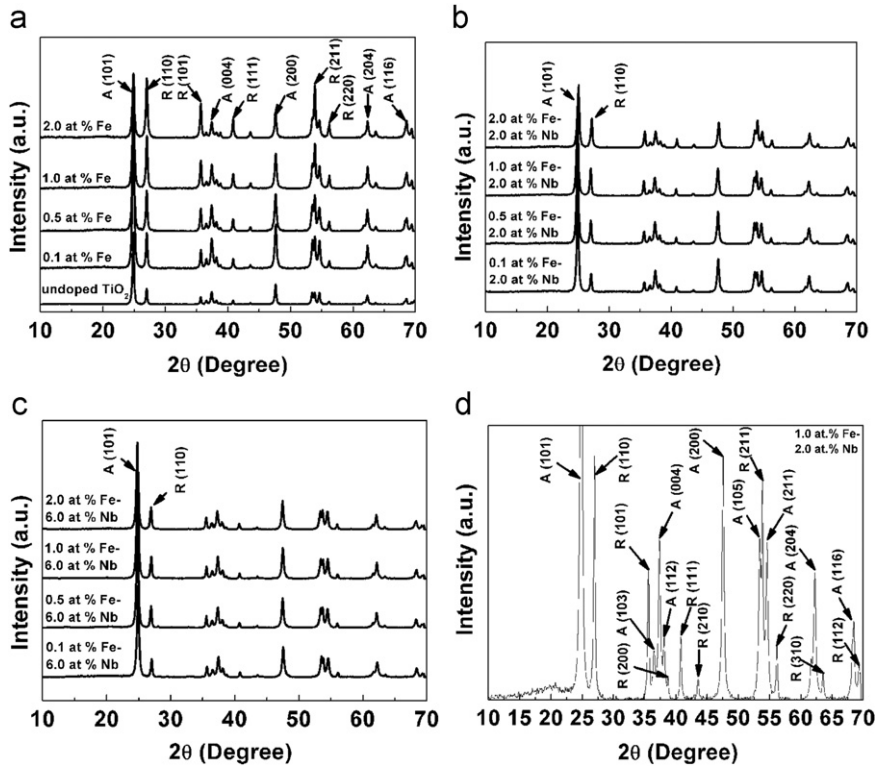

Fig. 2. XRD patterns of the plasma-synthesized powders: (a) TiO_2–Fe^{3+} (0–2.0 at%), (b) TiO_2–Fe^{3+} (0.1–2.0 at%)–Nb^{5+} (2.0 at%), (c) TiO_2–Fe^{3+} (0.1–2.0 at%)–Nb^{5+} (6.0 at%), and (d) TiO_2–Fe^{3+} (1.0 at%)–Nb^{5+} (2.0 at%). In Fig. (d), the *Y*-axis scale is ten-times more precise than those in other figures,(a)–(c). A and R denote anatase and rutile, respectively.

was prior to that of the rutile from the less undercooled ones, which would lead to larger rutile crystallites originating from more particle growth in such a process.

In this study, we could not find the peaks corresponding to any compounds related to iron or niobium in any of the XRD patterns (Fig. 2). This peak absence is attributed to relatively large solubilities of Fe^{3+} and Nb^{5+} dissolved into the TiO_2 lattice, due to their effective ionic radii (0.065 nm for Fe^{3+} and 0.064 nm for Nb^{5+}) being closely comparable to that (0.0605 nm) of Ti^{4+} [43]. The solubility of Fe^{3+} in previous study was more than $R_{Fe/Ti}=20\%$ via the thermal plasma synthesis [29] and that of Nb^{5+} was as high as ~25.0 at% in the Nb^{5+}-doped TiO_2 powders synthesized by the thermal plasma [44]. Such high solubilities for both Fe^{3+} and Nb^{5+} were seldom reported in the cases prepared by other wet-chemical techniques.

The intensities of the rutile (110) peaks relative to those of the anatase (101) ones steadily increased with the Fe^{3+} concentration (0–2.0 at%), as shown in Fig. 2a. This increased intensity was inhibited at 2.0 at% Nb^{5+} in the Nb^{5+}–Fe^{3+} codoped TiO_2 (Fig. 2b) and was almost negligible at 6.0 at% Nb^{5+} (Fig. 2c), implying that the Fe^{3+} doping promoted rutile formation whereas the Nb^{5+} introduction impeded rutile crystallization.

Evidence concerning the effects of Fe^{3+} and Nb^{5+} on the rutile formation is given in Fig. 3 through calculating rutile weight fraction according to Eq. (2). For the Fe^{3+}-doped TiO_2 powders, the rutile percentage dramatically increased from 19.9 wt% at 0 at% Fe^{3+} to 51.2 wt% at 20.0 at% Fe^{3+}. In contrast, with the Nb^{5+} addition, under the same conditions for the doped Fe^{3+} contents (0.1–2.0 at%), this enhanced tendency was much less dramatic. Especially, at 6.0 at% Nb^{5+} doping concentration, it only increased from 17.2 wt% at 0.1 at% Fe^{3+} to 22.4 wt% at 2.0 at% Fe^{3+}. To account for this phenomenon, there is an argument for the traditional crystal chemical that shared edges lead to cation–cation repulsion and structural destabilization in accordance with relative phase stability [29]. As anatase and rutile have quite different arrangements of structure-building blocks (Ti–O octahedrons) [16], as mentioned above, rutile with two shared edges therefore is more tolerant towards defects than anatase with four shared edges. This means that the oxygen vacancies created as the charge compensation in the TiO_2 host lattice due to the discrepancy between the chemical valences resulting from the substitution of Fe^{3+} for Ti^{4+} are mainly responsible for the rutile formation. This agrees with the finding reported by Vemury and Pratsinis [45] that rutile formation is enhanced either by introducing dopant oxides with the same crystal structure or by creating oxygen vacancies resulting from doping with subvalent cations such as Al^{3+}. Bechstein et al. [46] recently found similar findings in chromium-doped rutile TiO_2 that the enhanced formation of surface oxygen vacancies due to the chromium doping was in good agreement with a simple model based on maintaining charge neutrality while minimizing lattice stress. Therefore, we consider that the Nb^{5+} doping contributed to the inhibition of the rutile formation in this study by balancing the charge between Fe^{3+} and Ti^{4+}, which reduced the number of the oxygen vacancies created.

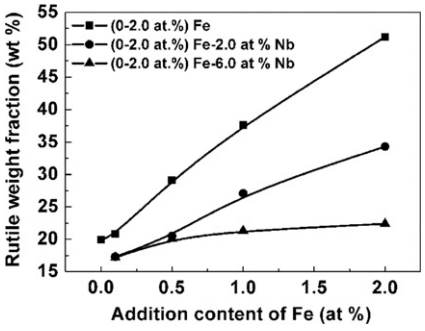

Fig. 3. Rutile weight fraction in the plasma-synthesized Nb^{5+}–Fe^{3+} codoped TiO_2 powders.

Some typical UV–vis absorption spectra are presented in Fig. 4a. Owing to the difference in their characteristic structures, the rutile band gap energy (E_g) of ~3.02 eV is smaller than that of anatase, ~3.23 eV [17]. The absorption onsets in the samples of TiO_2–Fe^{3+} (2.0 at%), TiO_2–Fe^{3+} (2.0 at%)–Nb^{5+} (2.0 at%) and TiO_2–Fe^{3+} (2.0 at%)–Nb^{5+} (6.0 at%) were clearly shifted to the visible light region, which is associated with the great differences in their rutile percentages (51.2, 34.3 and 22.4 wt%, respectively, as seen in Fig. 3).

The band gap energy (E_g) (Fig. 4b) was correspondingly estimated using Eqs. (3)–(5) from the UV–vis spectra (Fig. 4a). The verification on the accuracy of the E_g calculation was previously preceded [31] using Degussa P25 powder to obtain an indirect band gap of 2.87 eV, which is close to the calculated value of 2.91 eV corresponding to $X_{1a}\rightarrow G_{1b}$ indirect interband transition [47] and to the reported value of 2.95 eV [35]. The E_g values we calculated for the specimens of TiO_2–Fe^{3+} (2.0 at%) and TiO_2–Fe^{3+}(2.0 at%)–Nb^{5+} (6.0 at%) are ~2.26 and ~2.48 eV, respectively, indicating that the rutile percentage in the latter was larger than that in the former due to the Nb^{5+} doping. This is coincident with their rutile weight fractions of 22.4 wt% for the TiO_2–Fe^{3+} (2.0 at%)–Nb^{5+} (6.0 at%) and 51.2 wt% for the TiO_2–Fe^{3+} (2.0 at%) (Fig. 3), further verifying the contribution of Nb^{5+} doping to the inhibition of the rutile formation.

The particle morphologies in the plasma-synthesized powders as observed by FE-SEM are shown in Fig. 5 for some representative samples: (a) undoped TiO_2, (b) TiO_2–Fe^{3+} (2.0 at%), (c) TiO_2–Fe^{3+} (2.0 at%)–Nb^{5+} (2.0 at%) and (d) TiO_2–Fe^{3+} (2.0 at%)–Nb^{5+} (6.0 at%). They all demonstrate quite similarly featured morphology consisting

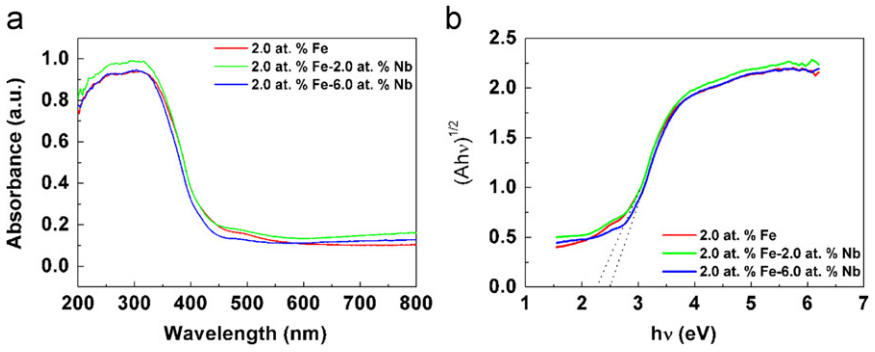

Fig. 4. . (a) Typical UV–vis absorption spectra of the plasma-synthesized Nb^{5+}–Fe^{3+} codoped TiO_2 powders and (b) correspondingly estimated band gap energies (E_g).

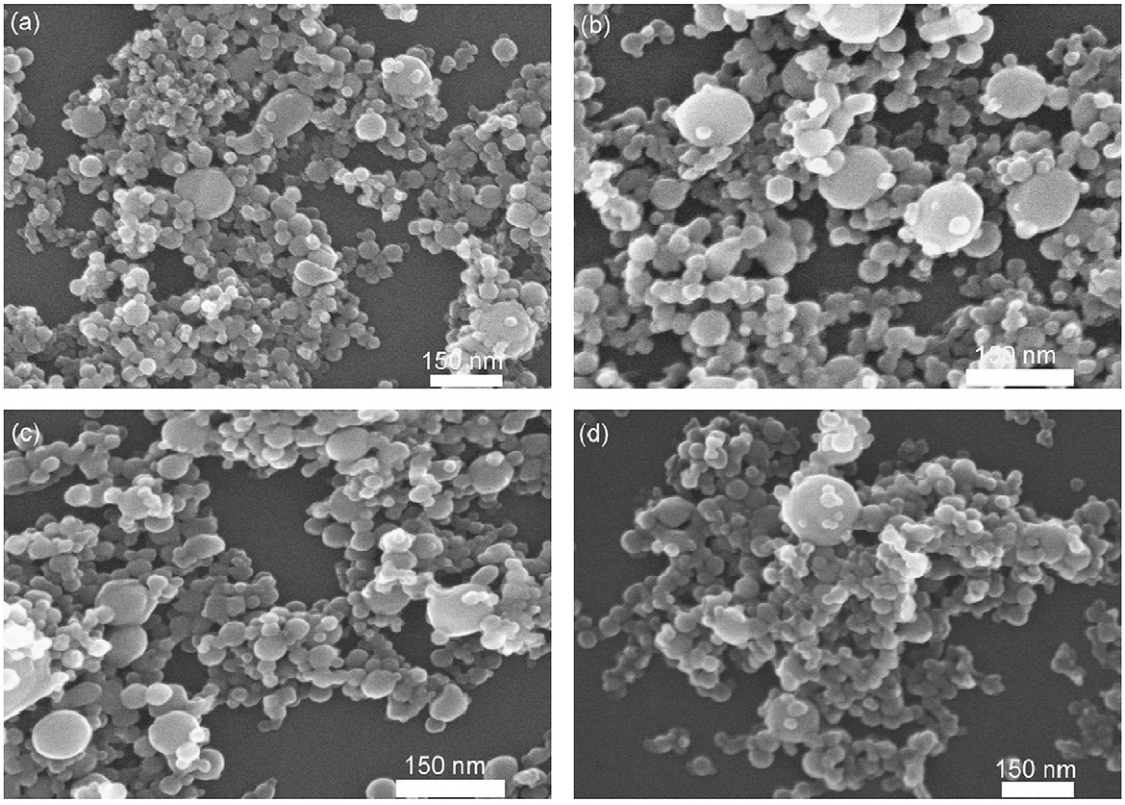

Fig. 5. FE-SEM images showing overall morphology of the plasma-synthesized powders: (a) undoped TiO_2, (b) TiO_2–Fe^{3+} (2.0 at%), (c) TiO_2–Fe^{3+} (2.0 at%)–Nb^{5+} (2.0 at%) and (d) TiO_2–Fe^{3+} (2.0 at%)–Nb^{5+} (6.0 at%).

of a majority of nano-sized particulates in faceted shape and a small proportion of submicrometer-sized crystals in nearly sphere. This morphology should be attributed to the different trajectories of the precursor mist droplets during the process of the thermal plasma synthesis. Namely, fine particles were produced via gas–solid route while large ones were formed via gas–liquid–solid path. To distinguish this featured morphology more clearly, typical TEM image of TiO_2–Fe^{3+} (0.1 at%)–Nb^{5+} (6.0 at%) is demonstrated in Fig. 6a. The well-dispersed powders distinguishably presented the morphology composition of a great many faceted nanometer particles and a few nearly spherical submicrometer ones. HRTEM analysis through identifying lattice space (Fig. 6b) confirms that the plasma-synthesized powders were composed of anatase and rutile polymorphs, as identified from the XRD patterns (Fig. 2).

The dependence of magnetization on magnetic-field measured at 300 K for the plasma-synthesized Nb^{5+}–Fe^{3+} codoped TiO_2 powders was plotted in Fig. 7: (a1) (0–10.0 at%) Nb^{5+}–(0.1 at%) Fe^{3+} and (b1) (6.0 at%) Nb^{5+}–(0.1–2.0 at%) Fe^{3+}. Both the magnetization curves were apparently superposed by paramagnetic and ferromagnetic components, with the former becoming predominant when applying magnetic field above about 3000 Oe.

The paramagnetic and ferromagnetic components, $M_{ferro.}$ and $M_{para.}$, of the magnetization can be separated each other. As shown in Fig. 7(a1) weak ferromagnetic property was observed from the hysteresis loop in the magnetic field below 3000 Oe. As metallic impurities have been precluded in this work, as evidenced by the XPS spectra (Fig. 1) and XRD patterns (Fig. 2), the paramagnetic and ferromagnetic properties can be reasonably ascribed to the intrinsic nature of the plasma-synthesized powders in this study. As shown in Fig. 7(b1) the ferromagnetic property gradually weaken with increase in Fe^{3+} content from 0.1 to 2.0 at% while Nb^{5+} content was kept at 6.0 at%. The saturation magnetization (M_s) and coercive force (H_c) obtained

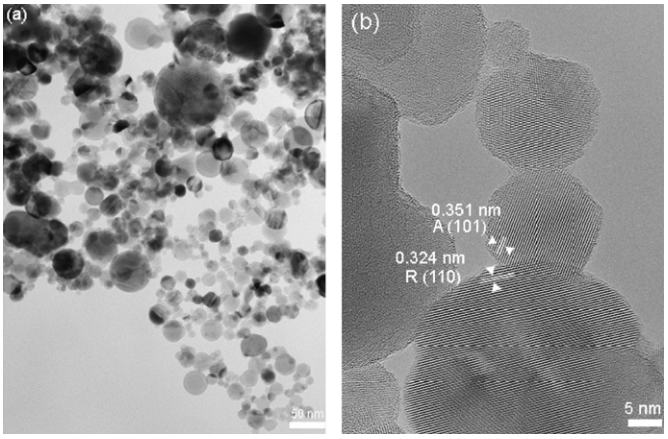

Fig. 6. TEM micrographs showing morphology of the plasma-synthesized (6.0 at%) Nb^{5+}–(0.1 at%) Fe^{3+} codoped TiO_2 powders: (a) overall particle morphology and (b) HRTEM lattice fringe of individual anatase and rutile nanocrystals.

from the ferromagnetic components (Fig. 7(a1) and (b1)) are plotted in Fig. 7(a2) and (b2). The M_s and H_c remained almost invariable for (0–10.0 at%) Nb^{5+}–(0.1 at%) Fe^{3+} (Fig. 7(a2)) but slightly decreased for (6.0 at%) Nb^{5+}–(0.1–2.0 at%) Fe^{3+} (Fig. 7(b2)), respectively, with various concentrations of the Nb^{5+} and Fe^{3+} dopants.

Moreover, the M_s values for all the samples were ~0.05 emu/mol for various Nb^{5+} concentrations (0–10.0 at%) and an Fe^{3+} molar ratio of 0.1 at%, corresponding to ~0.2% of $5N_A\mu_B$, calculated using

$$M_s = N_A \mu_B g S \tag{6}$$

where N_A, g and μ_B are the Avogadro number, the g factor (=2) and the Bohr magneton, respectively. This is the theoretical value from

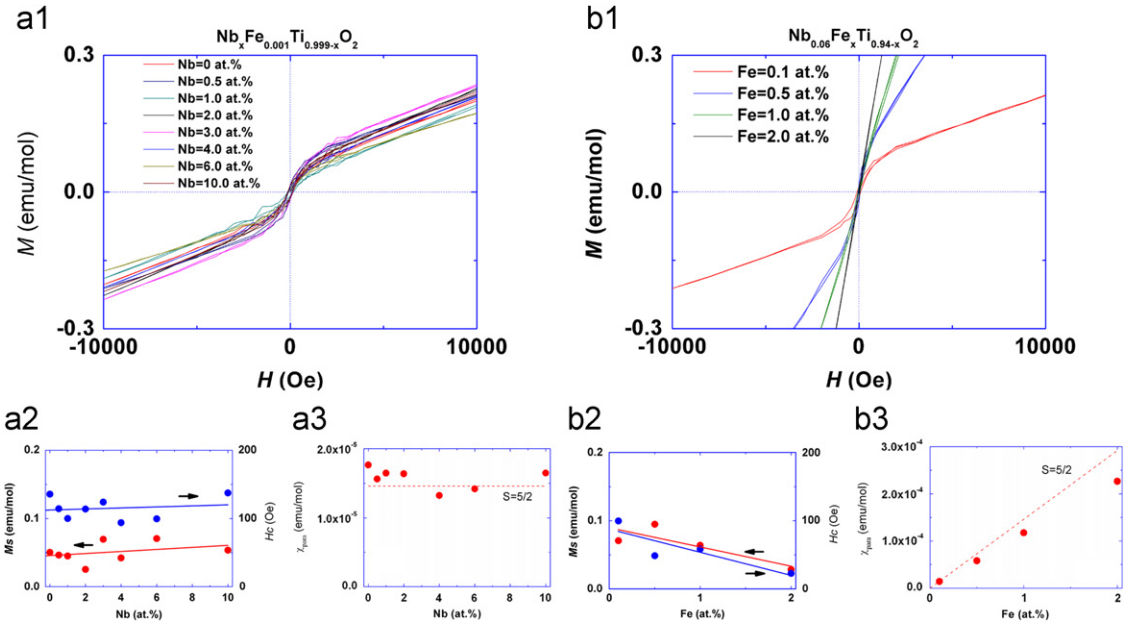

Fig. 7. Magnetization curves of the plasma-synthesized Nb^{5+}–Fe^{3+} codoped TiO_2 powders measured at 300 K: (a1) (0–10.0 at%) Nb^{5+}–(0.1 at%) Fe^{3+} and (b1) (6.0 at%) Nb^{5+}–(0.1–2.0 at%) Fe^{3+}. Corresponding saturation magnetization (M_s) and coercive force (H_c) are demonstrated in (a2) and (b2) and corresponding paramagnetic susceptibility ($\chi_{para.}$) is exhibited in (a3) and (b3), respectively.

the contribution of the Fe^{3+} spins at $S=5/2$. We can recognize that the contribution of Fe^{3+} to the ferromagnetization is quite small. For the paramagnetic part, it should mostly originate from the lone (or weakly correlated) Fe^{3+} spins ($S=5/2$: high spin state). The magnetic susceptibility, $\chi_{para.}=M_{para.}/H$, evaluated from the paramagnetic components, was plotted in Fig. 7(a3) and (b3). The dotted lines were calculated using the Curie law:

$$\chi_{para.}=\frac{C}{T} \tag{7}$$

where C is the Curie constant. As the theoretical C values for the total spin angular momentum at $S=5/2$ were evaluated using

$$C=\frac{c_{Fe}N_A S(S+1)g^2\mu_B^2}{3k_B} \tag{8}$$

the c_{Fe} values were assumed to be the molar ratio of Fe, as the contribution of the ferromagnetic part to the total magnetization was quite small. The $\chi_{para.}$ plots are almost the same as those evaluated from the theoretical C value. In the Supporting Information, the ferromagnetic and paramagnetic properties discussed here were confirmed in the temperature dependence of magnetization. The temperature dependence data was entirely consistent with the magnetization data at 300 K in Fig. 7.

Fukumura et al. [48] found that the strong ferromagnetic exchange coupling between localized spins is due to carrier-induced ferromagnetism, indicating the importance of the carrier concentration and mobility in the ferromagnetic performance of the DMS materials [17]. As a consequence, in this study, the weakening of the ferromagnetic with the increased Fe^{3+} content (Fig. 7(b1)) may be achieved by phase composition as a carrier-mediated exchange, since the carrier mobility in rutile is 0.05–0.2 $cm^2/V\,s$ much lower than that of 6–10 $cm^2/V\,s$ in anatase [17]. For the (6.0 at%) Nb^{5+}–(0.1–2.0 at%) Fe^{3+} codoped TiO_2 sample, the rutile percentage was 17.2, 20.1, 21.3 and 22.4 wt% at Fe^{3+} concentrations of 0.1, 0.5, 1.0 and 2.0 at%, respectively, as shown in Fig. 3, leading to lower carrier mobility at a higher Fe^{3+} doping level. This further confirms the proposed mechanism that ferromagnetism is a carrier-mediated exchange in DMS materials [18].

In our experiments, however, stronger ferromagnetic properties were not obtained all the time. Because conduction electrons were reported to play an essential role in the ferromagnetization of codoped TiO_2 fabricated at relatively low oxygen partial pressure (1×10^{-5} Torr) [49], the possible reason for the weak ferromagnetism in the plasma-synthesized Nb^{5+}–Fe^{3+} codoped TiO_2 powders may be related to the reduced number of conduction electrons, due to the similar electronic configurations of Co and Fe. In the present work, the emission of electrons in the conduction band might have been affected by the induced impurity states in the band gap due to the creation of interstitial oxygen [50], which readily formed due to the valence discrepancy between Nb^{5+} and Ti^{4+} [51], especially more readily at an oxygen atmosphere employed in the thermal plasma processing.

4. Conclusions

Radio-frequency thermal plasma was utilized to synthesize Nb^{5+}–Fe^{3+} codoped TiO_2 nanoparticles by oxidizing liquid precursor mist with various concentrations of Fe^{3+} (Fe/(Ti+Fe+Nb)=0–2.0 at%) and Nb^{5+} (Nb/(Ti+Fe+Nb)=0–10.0 at%). All the plasma-synthesized powders consisted of a mixture of anatase (major phase) and rutile polymorphs, without any evident metal or magnetic impurity phases. The average crystallite size (30–40 nm) of the anatase was smaller than that (56–74 nm) of the rutile. The rutile weight fraction was increased by the Fe^{3+} doping but was decreased by the Nb^{5+} addition. The amount of the anatase in the phase composition affected the band gap energy of the TiO_2 host lattice. All the resultant powders had similarly featured morphology of a majority of nano-sized particles in faceted shape and a small proportion of submicrometer-sized crystals in nearly sphere. The plasma-synthesized Nb^{5+}–Fe^{3+} codoped TiO_2 powders were prominently paramagnetic as well as weakly ferromagnetic in nature at room temperature. Increase in the Fe^{3+} content led to gradual decrease in the ferromagnetic property, supporting the report that the ferromagnetism is sensitive to the carrier concentration.

Acknowledgments

We are grateful to Satoshi Takenouchi and Kei Yamada for the chemical analysis. This work was partially supported by KAKENHI, a Grant-in-Aid for Scientific Research (B 19360334) from the Japan Society for the Promotion of Science.

Appendix A. Supplementary materials

Supplementary data associated with this article can be found in the online version at doi:10.1016/j.jssc.2011.07.025.

References

[1] T. Dietl, Acta Phys. Pol. A 100 (2001) 139–151.
[2] J. De Boeck, W. Van Roy, J. Das, V. Motsnyi, Z. Liu, L. Lagae, H. Boeve, K. Dessein, G. Borghs, Semicond. Sci. Technol. 17 (2002) 342–354.
[3] R.K. Zheng, M.P. Moody, B. Gault, Z.W. Liu, H. Liu, S.P. Ringer, J. Magn. Magn. Mater. 321 (2009) 935–943.
[4] A.J. Drew, J. Hoppler, L. Schulz, F.L. Pratt, P. Desai, P. Shakya, T. Kreouzis, W.P. Gillin, A. Suter, N.A. Morley, V.K. Malik, A. Dubroka, K.W. Kim, H. Bouyanfif, F. Bourqui, C. Bernhard, R. Scheuermann, G.J. Nieuwenhuys, T. Prokscha, E. Morenzoni, Nat. Mater. 8 (2009) 109–114.
[5] X.J. Wang, I.A. Buyanova, F. Zhao, D. Lagarde, A. Balocchi, X. Marie, C.W. Tu, J.C. Harmand, W.M. Chen, Nat. Mater. 8 (2009) 198–202.
[6] P. Sharma, A. Gupta, K.V. Rao, F.J. Owens, R. Sharma, R. Ahuja, J.M.O. Guillen, B. Johansson, G.A. Gehring, Nat. Mater. 2 (2003) 673–677.
[7] T. Jungwirth, J. Sinova, J. Masek, J. Kucera, A.H. MacDonald, Rev. Mod. Phys. 78 (2006) 809–864.
[8] D. Kitchen, A. Richardella, J.M. Tang, M.E. Flatte, A. Yazdani, Nature 442 (2006) 436–439.
[9] J.S. Kulkarni, O. Kazakova, J.D. Holmes, Appl. Phys. A—Mater 85 (2006) 277–286.
[10] Z.H. Zhang, X.F. Wang, J.B. Xu, S. Muller, C. Ronning, Q. Li, Nat. Nanotechnol 4 (2009) 523–527.
[11] S.A. Chambers, Surf. Sci. Rep. 61 (2006) 345–381.
[12] Y. Matsumoto, M. Murakami, T. Shono, T. Hasegawa, T. Fukumura, M. Kawasaki, P. Ahmet, T. Chikyow, S. Koshihara, H. Koinuma, Science 291 (2001) 854–856.
[13] Y. Matsumoto, R. Takahashi, M. Murakami, T. Koida, X.J. Fan, T. Hasegawa, T. Fukumura, M. Kawasaki, S.Y. Koshihara, H. Koinuma, Jpn. J. Appl. Phys. 40 (2001) L1204–L1206.
[14] M. Murakami, Y. Matsumoto, T. Hasegawa, P. Ahmet, K. Nakajima, T. Chikyow, H. Ofuchi, I. Nakai, H. Koinuma, J. Appl. Phys. 95 (2004) 5330–5333.
[15] U. Diebold, Surf. Sci. Rep. 48 (2003) 53–229.
[16] A.F. Wells, Structural Inorganic Chemistry, Clarendon Press, Oxford, 1975.
[17] T. Fukumura, H. Toyosaki, Y. Yamada, Semicond. Sci. Technol 20 (2005) S103–S111.
[18] T. Hitosugi, G. Kinoda, Y. Yamamoto, Y. Furubayashi, K. Inaba, Y. Hirose, K. Nakajima, T. Chikyow, T. Shimada, T. Hasegawa, J. Appl. Phys. 99 (2006) 08M121.
[19] S. Ramachandran, A. Tiwari, J. Narayan, Appl. Phys. Lett. 84 (2004) 5255.
[20] H. Pan, J.B. Yi, L. Shen, R.Q. Wu, J.H. Yang, J.Y. Lin, Y.P. Feng, J. Ding, L.H. Van, J.H. Yin, Phys. Rev. lett. 99 (2007) 127201.
[21] Q. Xu, H. Schmidt, S. Zhou, K. Potzger, M. Helm, H. Hochmuth, M. Lorenz, A. Setzer, P. Esquinazi, C. Meinecke, Appl. Phys. Lett. 92 (2008) 082508.
[22] H. Toyosaki, T. Fukumura, Y. Yamada, K. Nakajima, T. Chikyow, T. Hasegawa, H. Koinuma, M. Kawasaki, Nat. Mater. 3 (2004) 221.
[23] J.H. Park, M.G. Kim, H.M. Jang, S. Ryu, Y.M. Kim, Appl. Phys. Lett. 84 (2004) 1338.
[24] J.H. Kim, H. Kim, D. Kim, Y.E. Ihm, W.K. Choo, J. Appl. Phys. 92 (2002) 6066.
[25] S. Deka, P.A. Joy, Appl. Phys. Lett. 89 (2006) 032508.
[26] J. Hays, A. Thurber, K.M. Reddy, A. Punnoose, M.H. Engelhard, J. Appl. Phys. 99 (2006) 08M123.
[27] K.P. Bhatti, S. Chaudhary, D.K. Pandya, S.C. Kashyap, J. Appl. Phys. 101 (2007) 103919.
[28] T. Ishigaki, J.G. Li, Sci. Technol. Adv. Mat 8 (2007) 617–623.
[29] X.H. Wang, J.G. Li, H. Kamiyama, M. Katada, N. Ohashi, Y. Moriyoshi, T. Ishigaki, J. Am. Chem. Soc. 127 (2005) 10982–10990.
[30] J.G. Li, R. Buechel, M. Isobe, T. Mori, T. Ishigaki, J. Phys. Chem. C 113 (2009) 8009–8015.
[31] J.G. Li, M. Ikeda, C.C. Tang, Y. Moriyoshi, H. Hamanaka, T. Ishigaki, J. Phys. Chem. C 111 (2007) 18018–18024.
[32] R. Ye, T. Ishigaki, J. Jurewicz, P. Proulx, M.I. Boulos, Plasma Chem. Plasma Process. 24 (4) (2004) 555–571.
[33] K.P. Kumar, K. Keizer, A.J. Burggraaf, T. Okubo, H. Nagamoto, J. Mater. Chem. 3 (1993) 1151–1159.
[34] R.A. Spurr, H. Myers, Anal. Chem. 29 (1957) 760–762.
[35] J.C. Yu, J.G. Yu, W.K. Ho, Z.T. Jiang, L.Z. Zhang, Chem. Mater. 14 (2002) 3808–3816.
[36] J.D. Zhang, S. Fung, L. Li-Bin, L. Zhi-Jun, Surf. Coat. Technol. 158 (2002) 238–241.
[37] C.R. Cho, J.P. Kim, J.Y. Hwang, S.Y. Jeong, Y.G. Joh, D.H. Kim, Jpn. J. Appl. Phys. 43 (2004) L1323–L1326.
[38] E.E. Latta, M. Ronay, Phys. Rev. Lett. 53 (1984) 948–951.
[39] D. Morris, Y. Dou, J. Rebane, C.E.J. Mitchell, R.G. Egdell, D.S.L. Law, A. Vittadini, M. Casarin, Phys. Rev. B 61 (2000) 13445–13457.
[40] C.L. Qiu, L. Liu, M. Sun, S.M. Zhang, J. Biomed. Mater. Res. A 75 (2005) 950–956.
[41] P.C.J. Graat, M.A.J. Somers, Appl. Surf. Sci. 100 (1996) 36–40.
[42] Y.L. Li, T. Ishigaki, J. Cryst. Growth 242 (2002) 511–516.
[43] R.D. Shannon, Acta Crystallogr. A 32 (1976) 751–767.
[44] C. Zhang, M. Ikeda, T. Uchikoshi, J.G. Li, T. Watanabe, T. Ishigaki, J. Mater. Res. 26 (2011) 658–671.
[45] S. Vemury, S.E. Pratsinis, J. Am. Ceram. Soc. 78 (1995) 2984–2992.
[46] R. Bechstein, M. Kitta, J. Schutte, A. Kuhnle, H. Onishi, J. Phys. Chem. C 113 (2009) 3277–3280.
[47] N. Daude, C. Gout, C. Jouanin, Phys. Rev. B 15 (1977) 3229–3235.
[48] T. Fukumura, Y. Yamada, H. Toyosaki, T. Hasegawa, H. Koinuma, M. Kawasaki, Appl. Surf. Sci. 223 (2004) 62–67.
[49] G. Kinoda, T. Hitosugi, Y. Yamamoto, Y. Furubayashi, K. Inaba, Y. Hirose, T. Shimada, T. Hasegawa, Jpn. J. Appl. Phys. 45 (2006) L387–L389.
[50] H. Kamisaka, T. Hitosugi, T. Suenaga, T. Hasegawa, K. Yamashita, J. Chem. Phys. 131 (2009) 034702.
[51] F.A. Kroger, H.J. Vink, Solid State Phys. 3 (1956) 307–435.